Supporting Information

Nanostructured ZIF-67/$LaFeO_3$ p-n Heterojunction Interface for Amplified Cefotaxime Sensing & Intensified Photo-Fenton Degradation

Monalisa Samal[a], Dakshita Snud Sharma[b], Dharitri Rath[b], Jagannath Panda[c], P.G.R. Achary [a], Binita Nanda [a]*

[a]Department of Chemistry, Faculty of Engineering and Technology (ITER), Siksha O Anusandhan (Deemed to be) University, Bhubaneswar, Odisha, India-751 030

[b]Department of Chemical Engineering, Indian Institute of Technology Jammu (IIT), Jagti, Jammu – 181 221, Jammu and Kashmir, India

[c]Department of Chemistry, NIST University, Institute Park, Pallur Hills, Berhampur, India.

**Correspondence: binitananda@soa.ac.in*

1. Synthesis

1.1 Synthesis of ZIF-67

To synthesize ZIF-67, we dissolved 7.5 mmol (0.616 g) of dimethylimidazole and 2 mmol (0.582 g) of Co $(NO_3)_2.6H_2O$ separately in 25 mL of methanol. A rapid colour changes from dark red to blue-violet was observed upon introducing the dimethylimidazole solution into the cobalt nitrate solution with constant stirring, indicating the formation of ZIF-67. On order to ensure a full reaction, the mixture was stirred for 24 hours. The precipitate was then extracted by centrifugation, completely cleaned three times with anhydrous ethanol, and dried for 12 hours at 60^0C. The resultant blue-violet powder confirms the successful synthesis of ZIF-67, which is consistent with stirring based techniques that have been previously documented[1].

1.2 Synthesis of $LaFeO_3$

To synthesize bare $LaFeO_3$, in 50 mL of deionized water, we dissolved 2 mmol Fe $(NO_3)_3.9H_2O$, 2 mmol La $(NO_3)_3.6H_2O$, and 4 mmol citric acid to create bare $LaFeO_3$. We stirred the solution for an hour before gradually adding aqueous ammonia to get the pH down to 7. After reaching 70^0C, the mixture was heated and stirred for 4 more hours. A yellow aerogel was then produced by drying the mixture for 10 hours at 90^0C. In order to get the bare $LaFeO_3$ product, this precursor was finally calcined in air for 2 hours at 500^0C[2].

1.3 Synthesis of ZIF-67/$LaFeO_3$

To synthesize the ZIF-67/$LaFeO_3$ nanocomposite, 200 mg of pre-synthesised $LaFeO_3$ and 2.9 g of cobalt nitrate hexahydrate [Co $(NO_3)_2.6H_2O$] were meticulously measured and then completely

dissolved in 25 mL of methanol. After that, this combination was sonicated to ensure a uniform dispersion. Meanwhile, 6.57 g of 2-methylimidazole were dissolved in 20 mL of methanol in a different vessel to create solution B. After preparing both solutions, solution B was gradually and carefully added to solution A while being continuously sonicated for half an hour. This intense sonication guaranteed close mixing of the precursors and aided the reaction. The solid outcome of the sonication process was carefully separated. Any unreacted precursors or byproducts were successfully eliminated by putting the product through three consecutive cycles of washing with new methanol in order to purify it. The next step was to dry the purified product for 6 hours at 70^0 C in an oven to produce the required substance.

1.4 Photocatalytic degradation of antibiotic Cefotaxime (CFX) degradation

In order to analyse photo-Fenton degradation, CFX was used as a common model pollutant. A conical flask was filled with 20 mL of CFX solution and 0.02 g of the catalyst to start the experiment. The adsorption-desorption equilibrium was then established by stirring this mixture for 30 minutes in the dark. A certain quantity of H_2O_2 was added to the catalyst mixed CFX solution prior to exposure to sunlight. Following the degradation test, the suspension was filtered, and a Jasco V-750 UV-vis spectrophotometer set to 260 nm was used to measure the amount of CFX in the solution. Ultimately, the following formula was used to determine the CFX degradation rate.

$$\eta = \frac{C_0 - C_t}{C_0} \times 100\% = \frac{A_0 - A_t}{A_0} \times 100\% \quad \textbf{(1)}$$

In this case, C_0 and A_0 stands for the original CFX concentration and absorbance, respectively, and C_t and A_t for the post-reaction values.

1.5 Electrochemical sensing of CFX

Cyclic voltametric measurements (CV) were performed with different doses of CFX in 40 mM Britton-Robinson (BR) buffer at pH 6.0, which was chosen as the ideal setting. By recording the current response at a scan rate of 0.1 V/s^{-1} throughout a potential range of 6.0 V to 1.2 V, the redox properties of CFX at the constructed electrochemical sensor were revealed. CFX concentrations and baseline-corrected were correlated to create calibration graphs.

1.6 Electrochemical sensing of CFX

ZIF-67, $LaFeO_3$, and ZIF-67/$LaFeO_3$ nanocomposites were synthesized as described in the synthesis section and used to modify screen-printed carbon electrodes (SPCEs) by drop-casting a dispersion of the nanocomposite onto the working electrode surface, followed by drying at room temperature. The modified SPCE was used as the working electrode, Ag/AgCl as the reference electrode, and a Pt wire as the counter electrode in a traditional three-electrode setup for electrochemical experiments. Initially,

interfacial charge-transfer properties were assessed using cyclic voltammetry (CV) in 0.1 M KCl containing 5 mM [Fe (CN)6] $^{3-/4-}$.

1.7 Photodegradation of CFX via photo-Fenton process

To reach adsorption-desorption equilibrium, aqueous solutions of CFX at the 20-ppm concentration were combined with ZIF-67, $LaFeO_3$, or ZIF-67/$LaFeO_3$ photocatalysts. The mixtures were then agitated in the dark for 10 minutes. A catalyst dosage of 20 mg and an H_2O_2 concentration of 10 mM were used in the photodegradation processes, which were conducted in a total volume of 20 mL with continuous stirring. The drug solution was subjected to a light source with a wavelength range of 200-500 nm and an intensity of around 1,000,000 lx, as determined by a TES 1332A light meter (Taiwan). To maximize degrading efficiency, key operating parameters such as catalyst loading, pH (2-8), H_2O_2 volume, and starting CFX concentration were methodically tuned. A pseudo-first-order model was used to investigate the degradation kinetics and track residual CFX concentrations on a regular basis.

2. Result and discussion

Table-S1 Surface area, total pore volume and pore size of ZIF-67, $LaFeO_3$, and ZIF-67/$LaFeO_3$.

Materials	Specific surface area (m^2/g)	Total pore volume (cc/g)	Pore size (nm)
ZIF-67	1181.41	6.2903	1.56
$LaFeO_3$	3.31482	1.6687	4.31
ZIF-67/$LaFeO_3$	1082.94	6.0278	1.82

Table-S2 Specific capacitance of all the materials at different scan rates.

Specific Capacitance at different scan rate						
Samples	**10mV/s**	**20mV/s**	**30mV/s**	**40mV/s**	**50mV/s**	**100mV/s**
ZIF-67	184	179.5	174.8	170.1	163.0	123.8
$LaFeO_3$	27.27	24.8	23.5	22.09	21.8	19.6
ZIF-67/$LaFeO_3$	182.2	151.1	131.1	118.1	111.3	74.7

2.1 Impedance analysis

Impedance spectroscopy was employed to investigate the dielectric and electrical properties of materials over wide frequency at room temperature using impedance analysis. The electrical response arises from contributions grains, grain boundaries, and interfacial effects, which govern the behaviour of bound and mobile charge carriers within the material. The complex impedance ($Z^* = Z' - iZ''$) consists of real (Z') and imaginary (Z'') components, expressed as:

$$Z^{'} = \frac{R}{1+(\omega\tau)^2} \; and \; Z'' = \frac{R\omega\tau}{1+(\omega\tau)^2} \qquad \textbf{(2)}$$

Where, τ=RC is the relaxation time, C and R are the capacitance and resistance respectively, and ω is the angular frequency of the electric field. The frequency dependent behaviour of the real (Z') and imaginary (Z'') components of impedance at elevated temperatures is depicted in **Fig.S1**. I can be seen Z' decreases markedly with increasing frequency, particularly at room temperature, indicating enhanced charge carrier mobility and increased electrical conductivity. This behaviour is characteristic of semiconducting materials exhibiting negative temperature coefficient of resistance (NTCR) [3]. At low frequencies, higher Z' values originate from charge accumulation at grain boundaries, which act as barriers to charge transport. As frequency increases, these barriers become less effective due to the rapid oscillation of the applied field, facilitating charge carrier motion.

On the other hand, **Fig.10b** displays the imaginary components (Z'') frequency dependency. It first rises with frequency, reaches a maximum (Z_{max}), and then falls. A peak in Z'' indicates a relaxation process, which is linked to localized charge carriers hopping across grain boundaries or between defect states. A reduction in relaxation time is shown by the shift of Z_{max} to higher frequencies with increasing temperature, which validates thermally stimulated conduction behaviour. Furthermore, space charge polarization contributions decrease at higher frequencies, and the bulk characteristics of material mostly control the impedance response. The electrical response of the material is mostly dependent on temperature and frequency, according to the impedance analysis. At low frequencies, it is controlled by grain boundary effects, while at higher frequencies, it is regulated by bulk conduction and relaxation dynamics. A better understanding of the conduction process of materials is essential for maximizing its performance in energy storage, sensors, and photocatalysis, among other applications. The actual component of impedance is defined by **Eq.3**:

$$Z' = \frac{R_b}{1+(\frac{\omega}{\omega_1})^m + (\frac{\omega}{\omega_2})^{-n}} \qquad \textbf{(3)}$$

Where $\omega_1 = 2\pi f_1$ and $\omega_2 = 2\pi f_2$ are the angular frequencies, R_b is the bulk resistance, ω is the applied variable frequency, and m and n are the exponents in the low frequency (f_2) and high frequency (f_1) regions, respectively. It is evident from the experimental results in **Fig.S1b** that the value of Z'' rises and then gradually lowers as the frequency rises, the system exhibits reduced responsiveness at high frequencies because of inertia or lag in the polarization processes, capacitive energy storage at low frequencies, and maximal energy dissipation at a characteristics frequency. Using a precise procedure, the reactance portion of the impedance is computed. As previously explained, the symbols have the same meaning.

$$Z'' = \frac{R_b}{1 + (\frac{\omega}{\omega_1})^{m'} + (\frac{\omega}{\omega_2})^{-n'}} \quad \textbf{(4)}$$

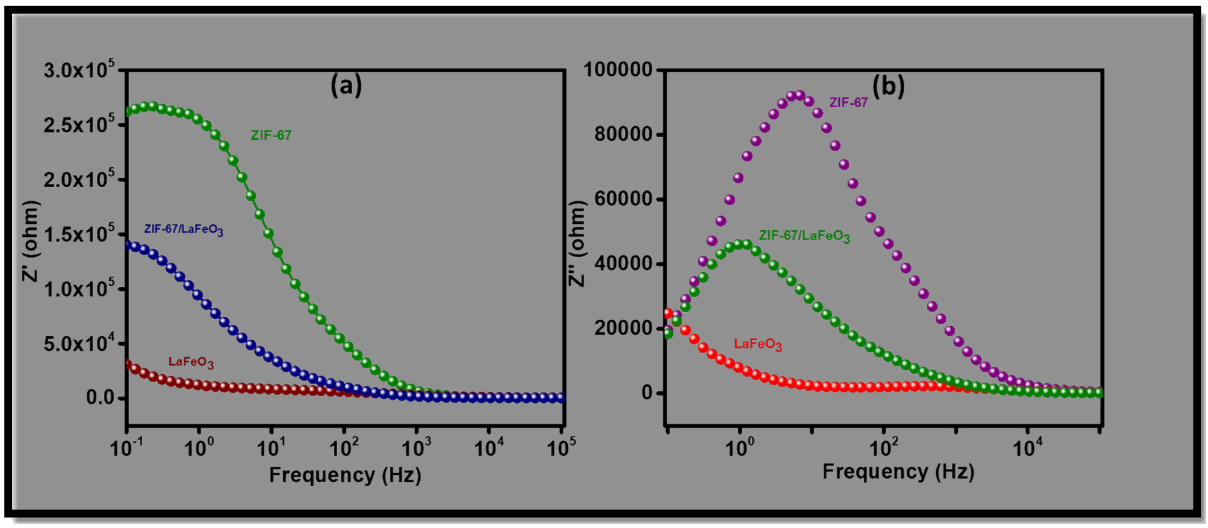

Fig.S1 (a) Variation of Z' with frequency, and (b) Z'' with frequency.

Table-S3 Circuit parameter data of all the materials at room temperature.

	Materials		
Parameters	**ZIF-67**	**$LaFeO_3$**	**ZIF-67/$LaFeO_3$**
L (Henry)	3.059×10^{-7}	3.204×10^{-7}	3.078×10^{-4}
R_b (ohm)	3.059×10^{-7}	3.59×10^{-3}	3.059×10^{-7}
Q ($S.sec^5/cm^2$)	4.939×10^{-6}	3.026×10^{-5}	2.808×10^{-6}
n	0.47	0.28	0.52
C_{gb} (F)	1.063×10^{-8}	1.22×10^{-6}	9.74×10^{-9}
R_{gb} (ohm)	1.568×10^{5}	1.22×10^{-10}	1.065×10^{6}

3. Photocatalytic activity for CFX degradation

A scavenging experiment was conducted using ZIF-67/$LaFeO_3$, as the model photocatalyst to identify the dominant reactive species responsible for its photocatalytic activity. Specific scavengers were employed to selectively quench certain reactive species: Citric acid for photogenerated holes (h^+), dimethyl sulfoxide (DMSO) for electrons (e^-), p-benzoquinone (PBQ) for superoxide radicals ($O_2^{\cdot-}$), and isopropanol (IPA) for hydroxyl radicals ($^{\cdot}OH$). The primary active species involved in the degradation pathway were determined by assessing the effect of each scavenger on the photocatalytic degradation efficiency, as shown in Fig. S2a. It was observed that the addition of PBQ, citric acid, and DMSO significantly inhibited the photocatalytic degradation of CFX, whereas IPA, which traps

hydroxyl radicals, had a comparatively lesser effect. These results indicate that h^+, e^-, and O_2 are the major reactive species responsible for CFX degradation.

The reusability and operational stability of the ZIF-67/$LaFeO_3$ nanocomposite were evaluated through consecutive degradation cycles under identical experimental conditions. In each cycle, a fixed amount of catalyst (0.02 g) was dispersed in 20 ppm of the CFX drug solution, maintaining the same reaction volume, light intensity, and oxidant concentration as used in the initial experiment. Centrifugation and washing were used to remove and isolate the catalyst after each cycle. After being dried in an oven, the recovered photocatalyst was put to further use. **Fig.S2b** illustrates the four sequential cycles of this degradation-regeneration mechanism. After four cycles, the CFX degradation rate decreased to 85.3%. Therefore, it has been verified that the photocatalytic activity of the catalysts did not significantly alter after each run. This demonstrates the strong photostability of the catalysts.

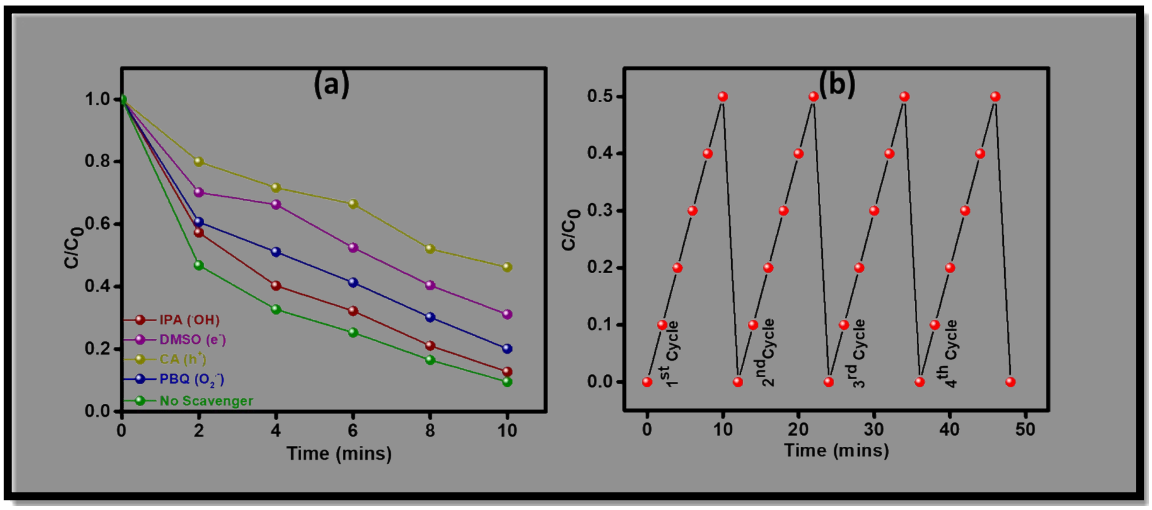

Fig.S2 (a) Impact of various scavenging agents, (b) reusability assessment of ZIF-67/$LaFeO_3$ composite.

Table-S4 The valence band (VB), conduction band (CB), and χ value of ZIF-67 and $LaFeO_3$.

Materials	**Absolute electronegativity (χ)**	**Band energy E_g (eV)**	**Valence band E_{VB} (Ev)**	**Conduction band E_{CB} (eV)**
ZIF-67	5.02	1.9	1.47	-0.43
$LaFeO_3$	5.5	2.3	2.14	-0.1

Table-S5 Degradation efficiencies, R^2, k_{app} and $t_{1/2}$ values of drug at different concentration towards CFX degradation.

SI No.	Target Antibiotic	Electrode/ sensor	Detection Technique	LOD	Ref
1.	CFX	Schiff base Zn (II) complex	DPV	0.1–100 µM	[4]
2.	CFX	AuNPs/Parg/CPE	CV and LSV	0.01–100.0 µM	[5]
3.	CFX	NaMM/ERGO/CPE	CV and DPV	0.1 nM	[6]
4.	CFX	Au-PDA@SiO_2/rGO/GCE	DPV	0.0001 µM	[7]
5.	CFX	Nano-Pd@ITO	Amperometry analysis	0.06 µM	[8]
6.	CFX	FeNP/GCE	DPV	0.1 µM	[9]
7.	CFX	MIP/GNWs@IL-PPNPs/COOH-rGO/GCE	DPV	0.0001 µM	[10]
8.	CFX	Au–PtNPs/MWCNT/GCE	LSV	0.001 µM	[11]
9.	**Cefixime**	**IL/$CoFe_2O_4$/rGO**	**DPV**	**0.035 µM**	**[12]**
10.	**CFX**	**ZIF-67/$LaFeO_3$/SPCE**	**CV**	**3.41 ppm/ 7.5 µM**	**Present work**

Table-S6 Comparative study of electrochemical sensing of CFX by different electrode.

Concentration of drug (ppm)	R^2	K_{app} (min^{-1})	$t_{1/2}$ (min)
20	0.98	0.1014	6.83
40	0.99	0.086	8.05
60	0.99	0.100	6.93
80	0.99	0.099	7
100	0.99	0.097	7.1

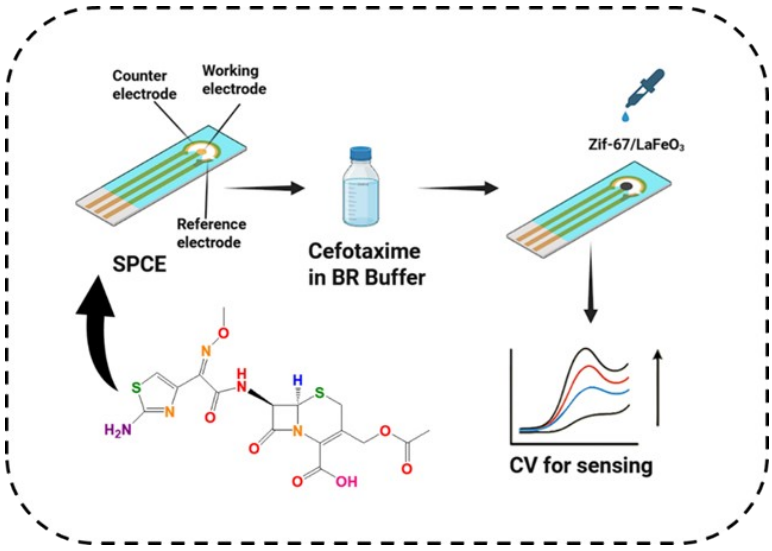

Scheme.S1 Schematic diagram of the synthesis procedure to form ZIF-67/$LaFeO_3$ electrode for sensing.

Table.S7 Identification of parent compound detected by HR-MS.

Sl. No.	m/z Value	Molecular Formula	Tentative Name
1	455	$C_{16}H_{17}N_5O_7S_2$	Cefotaxime
2	365	$C_{14}H_{15}N_5O_5S_2$	Deacetylated Cefotaxime
3	279	$C_{11}H_{13}N_3O_3S_2$	Thiazine-thiazole containing fragment
4	201	$C_8H_{11}N_3O_2S$	Aminothiazole-amide derivatives
5	100	$C_3H_4NS_2$	Thiazole fragment
6	102	$C_4H_6NS_2$	Methyl substituted thiazole fragment

4. Zeta Potential analysis

The zeta potential distribution profiles elucidate the evolution of surface charge upon composite formation. ZIF-67 exhibits a distribution centred at -20 to -30 mV, indicative of moderate electrostatic stabilization arising from its framework surface[13] **(Fig.S3)**. In contrast, $LaFeO_3$ shows a shift toward lower absolute zeta potential values (-10 to -20 mV), reflecting reduced surface charge density and an increased tendence toward aggregation. Additionally, the ZIF-67/$LaFeO_3$ composite exhibits a sharp distribution between 0 and -10 mV, indicating a significant alteration in the interfacial electrostatic environment. Strong heterointerface coupling and effective composite integration are confirmed by this near neutral surface charge, which results from interfacial charge compensation between ZIF-67 and

$LaFeO_3$. It is anticipated that under catalytic circumstances, such surface charge modulation will increase structural integrity and inhibit metal ion leaching, improving operational stability.

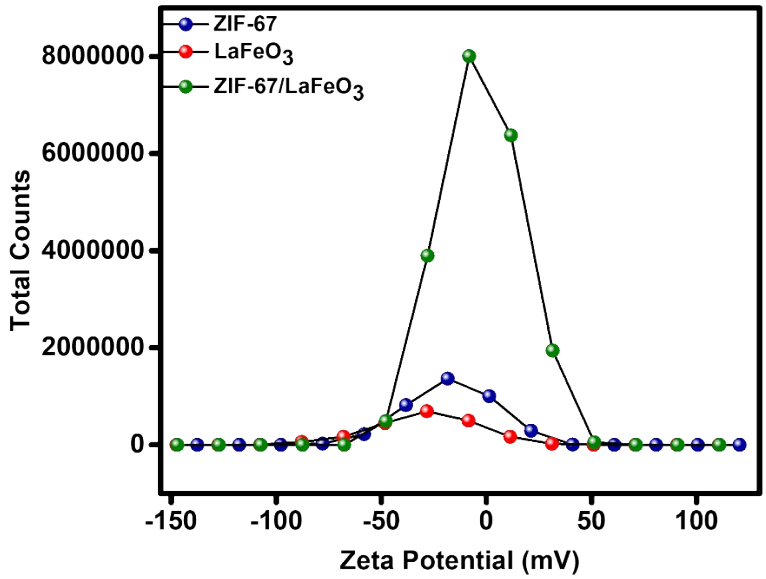

Fig.S3 Zeta potential of ZIF-67, $LaFeO_3$, and ZIF-67/$LaFeO_3$.

Abbreviations: GCE: Glassy carbon electrode, SPCE: Screen printed carbon electrode, MOF: Metal-organic framework, DPV: Differential pulse voltammetry, EIS: Electrochemical impedance spectroscopy, LSV: Linear sweep voltammetry, CV: Cyclic Voltammetry, CPE: Carbon paste electrode.

References

1 C. Gao, D. Li, Q. Wen, F. Song and J. Zhou, *Appl. Surf. Sci.*, 2024, **645**, 158872.

2 Y. Song, S. Xue, G. Wang, J. Jin, Q. Liang, Z. Li and S. Xu, *J. Phys. Chem. Solids*, 2018, **121**, 329–338.

3 W. Wieczorek, J. Płocharski, J. Przyłuski, S. Głowinkowski and Z. Pajak, *Solid State Ionics*, 1988, **28**, 1014–1017.

4 P. Nigam, S. Mohan, S. Kundu and R. Prakash, *Talanta*, 2009, **77**, 1426–1431.

5 F. Zhang, S. Gu, Y. Ding, L. Zhou, Z. Zhang and L. Li, *J. Electroanal. Chem.*, 2013, **698**, 25–30.

6 S. Dehdashtian, M. Behbahani and A. Noghrehabadi, *J. Electroanal. Chem.*, 2017, **801**, 450–458.

7 M. Z. H. Khan, M. Daizy, C. Tarafder and X. Liu, *Sci. Rep.*, 2019, **9**, 19041.

8 S. Gupta and R. Prakash, *Electroanalysis*, 2014, **26**, 2337–2341.

9 M. Wang, X. Xu, J. Yang, X. Yang and Z. Tong, *Micro \& Nano Lett.*, 2011, **6**, 284–288.

10 G. Yang, F. Zhao and B. Zeng, *Biosens. Bioelectron.*, 2014, **53**, 447–452.

11 S. Shahrokhian and S. Rastgar, *Analyst*, 2012, **137**, 2706–2715.

12 R. Darabi and M. Shabani-Nooshabadi, *J. Pharm. Biomed. Anal.*, 2022, **212**, 114657.

13 A. E. D. Mahmoud and R. Suri, *Water Sci. Eng.*